

Article

Micro-Ramps for Hypersonic Flow Control

Mohd R. Saad ¹, Hossein Zare-Behtash ², Azam Che-Idris ¹ and Konstantinos Kontis ^{2,*}

¹ Faculty of Engineering, Universiti Pertahanan Nasional Malaysia, Kuala Lumpur 57000, Malaysia; E-Mails: mohdrashdan.saad@postgrad.manchester.ac.uk (M.R.S.); azam.cheidris@postgrad.manchester.ac.uk (A.C.I.)

² School of Mechanical, Aerospace and Civil Engineering, University of Manchester, Manchester M13 9PL, UK; E-Mail: h.zare-behtash@manchester.ac.uk

* Author to whom correspondence should be addressed; E-Mail: k.kontis@manchester.ac.uk; Tel.: +44-0-161-306-9200; Fax: +44-0-161-306-3755.

Received: 3 March 2012; in revised form: 27 March 2012 / Accepted: 19 April 2012 /

Published: 26 April 2012

Abstract: Shock/boundary layer interaction (SBLI) is an undesirable phenomenon, occurring in high-speed propulsion systems. The conventional method to manipulate and control SBLI is using a bleed system that involves the removal of a certain amount of mass of the inlet flow to control boundary layer separation. However, the system requires a larger nacelle to compensate the mass loss, larger nacelles contribute to additional weight and drag and reduce the overall performance. This study investigates a novel type of flow control device called micro-ramps, a part of the micro vortex generators (VGs) family that intends to replace the bleed technique. Micro-ramps produce pairs of counter-rotating streamwise vortices, which help to suppress SBLI and reduce the chances of flow separation. Experiments were done at Mach 5 with two micro-ramp models of different sizes. Schlieren photography, surface flow visualization and infrared thermography were used in this investigation. The results revealed the detailed flow characteristics of the micro-ramp, such as the primary and secondary vortices. This helps us to understand the overall flow physics of micro-ramps in hypersonic flow and their application for SBLI control.

Keywords: micro-ramp; micro-vortex-generator; shock-boundary layer interaction; hypersonic; flow control

1. Introduction

Hypersonic aero-vehicles rely on optimum performance from their air-breathing propulsion system. However, the prominent problem faced by the propulsion system is the phenomenon known as shock wave-boundary layer interactions (SBLIs) which cause boundary layer separation and adverse pressure gradients, that eventually lead to total pressure loss and flow distortion in the intake section [1,2]. All of these reduce the overall propulsive efficiency of a hypersonic vehicle. Therefore, it is imperative to apply flow control mechanisms either at the beginning or throughout the interaction itself to prevent the boundary layer separation and at the same time maintain a high rate of efficiency even at off design conditions.

The micro-ramp is a recently developed novel flow control device [3–6]. It is a part of the micro-vortex generator family that has shown potential in solving the adverse phenomena. The term ‘micro’ refers to the device having a height smaller than the boundary layer thickness, δ . There has always been a never-ending dispute on the percentage of the micro-ramp height to δ of the flow, but in most of the literatures at present, the range is stated between 30% and 90% [5,7–10]. Because of the small size of the micro-ramps, it is embedded inside the boundary layer, which is intended to reduce the parasitic drag relative to the conventional full size vortex generator. Apart from this, the advantages that can be listed are cost-effectiveness, physically robustness and independence of power source.

The initial theory on utilizing micro-ramp in SBLIs problems was proposed by Babinsky *et al.* [11]. They conducted experimental investigations at Mach 2.5 based on the geometries of the micro-ramp suggested by Anderson *et al.* [7] in their numerical optimization studies. From their experiments it was found that the counter-rotating streamwise vortices generated by the micro-ramp, that travel downstream, helped to suppress the SBLIs’ effect and improve the state of the boundary layer by producing upwash and downwash motion. This motion transports the low-momentum flow at the wall surface to the outer regions of the boundary layer and simultaneously brings the high-momentum flow from the outer regions towards the wall surface. Therefore, a healthier and more robust boundary layer, which is less prone to separation, is created.

Later on Li & Liu [9,10] detailed the flow characteristics in the micro-ramp downstream region in their numerical investigation. A chain of vortex ring structures was identified originating from the apex of the micro-ramp due to Kelvin-Helmholtz instability [12–14]. These ring structures propagate further downstream and interact with the impinging shock wave, eventually distorting the structure of the shock wave hence reducing its strength [15]. The experiments of Lu *et al.* [16,17] and Sun *et al.* [18] corroborated the numerical findings of Li & Liu [9,10] and identified the existence of the vortex rings, however they were not able to shed any light on the effect of the interaction between the vortex rings with the impinging shock wave.

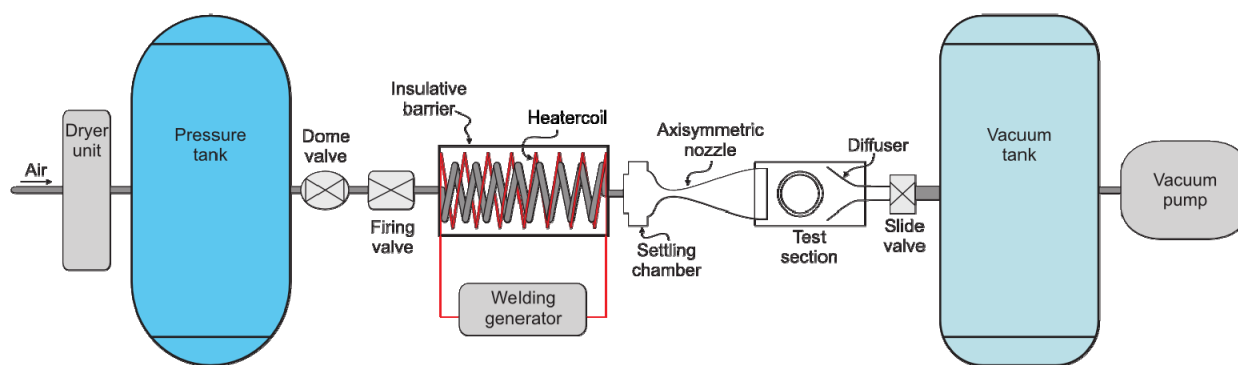
Since the majority of the studies on micro-ramps mentioned previously were done in supersonic conditions, it is essential to perform studies on the capability of micro-ramps in manipulating hypersonic flow and consequently improve the separated boundary layer caused by the incident shock. The results of this study are not only vital in understanding the efficiency of micro-ramps in hypersonic flow but also for the development and verification of numerical codes. The main objective of this study is to explore the behavior of the flow over and downstream the micro-ramp and its potential in suppressing turbulent boundary layer separation due to SBLIs at Mach 5.

2. Experimental Setup & Flow Diagnostics

2.1. High Supersonic Tunnel (HSST)

All the experiments were conducted at Mach 5 with a unit Reynolds number of $13.2 \times 10^6 \text{ m}^{-1}$ in the HSST, a hypersonic blow-down wind tunnel shown in Figure 1. The tunnel is identical to that used by Erdem *et al.* [19] and Yang *et al.* [20]. The operational stagnation pressure of the wind tunnel was set at $6.50 \times 10^5 \text{ Pa}$ ($\pm 5 \times 10^3 \text{ Pa}$) and a stagnation temperature of 375 K ($\pm 5 \text{ K}$). The freestream Reynolds number fluctuated at values no more than 3.7% and is considered sufficiently small. The Knudsen number of the flow was calculated to be a small value, 5.6×10^{-7} . Therefore, the flow was treated as a continuous medium.

Figure 1. Schematic layout of the Aero-Physics Laboratory high supersonic tunnel (HSST).



2.2. Micro-Ramps

In this investigation, two micro-ramp models named MR80 and MR40 were tested. Table 1 lists the detailed characteristics of the two models for comparison with reference to the micro-ramp diagram shown in Figure 2. MR80 and MR40 have heights of 80% and 40%, respectively, of the boundary layer thickness. At the micro-ramp location δ was estimated to be 5.89 mm. The boundary layer thickness is defined as the distance from the wall to a point where the velocity of the flow has essentially reached the freestream velocity, U_∞ . This was obtained from a preliminary investigation using high-speed schlieren images. The error for the value was calculated to be 1.4% of the overall thickness. The models were sized based on the design proposed by Anderson *et al.* [7] in their optimization investigation, where the ratio of dimensions are given as $s/h = 7.5$ and $c/h = 7.2$. They were machined on top of a metal strip and fixed to a 360 mm long, 60 mm wide and 5 mm thick aluminum alloy flat plate. Forty pressure tappings were installed downstream of the micro-ramp and connected to Kulite pressure transducers. The complete assembly of the micro-ramp with the flat plate is presented in Figure 3. A baseline model (plate without ramp) was also used and named MR00.

Table 1. Dimensions of MR80 and MR40 for comparison.

Dimensions (mm)	MR80	MR40
Height, h	4.64	2.32
Chord, c	33.4	16.7
Width, w	27.2	13.6

Figure 2. Diagram of a micro-ramp showing the dimensions.

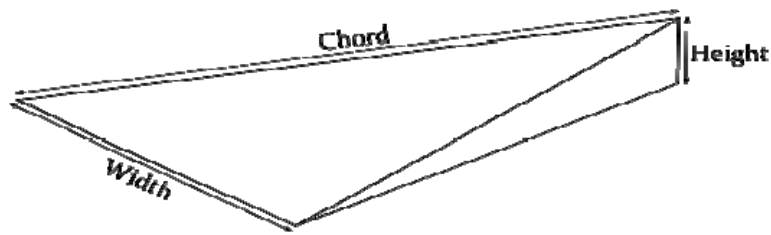
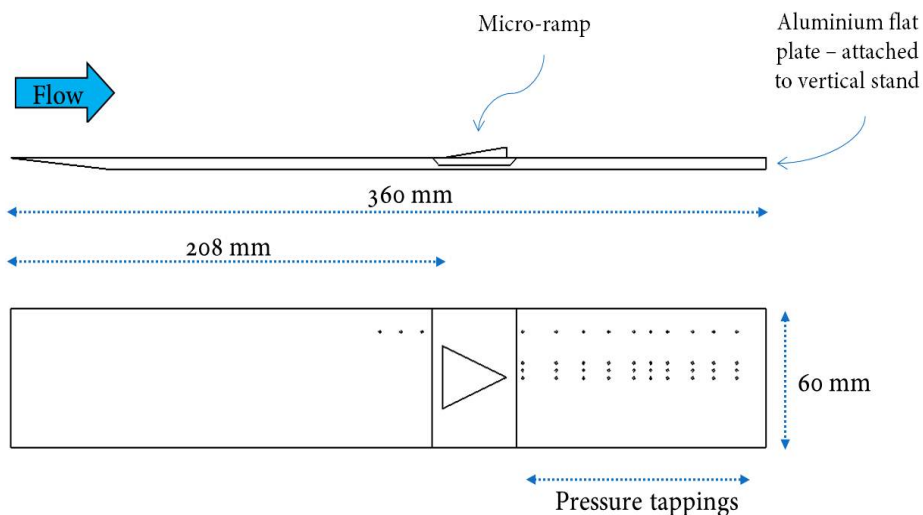
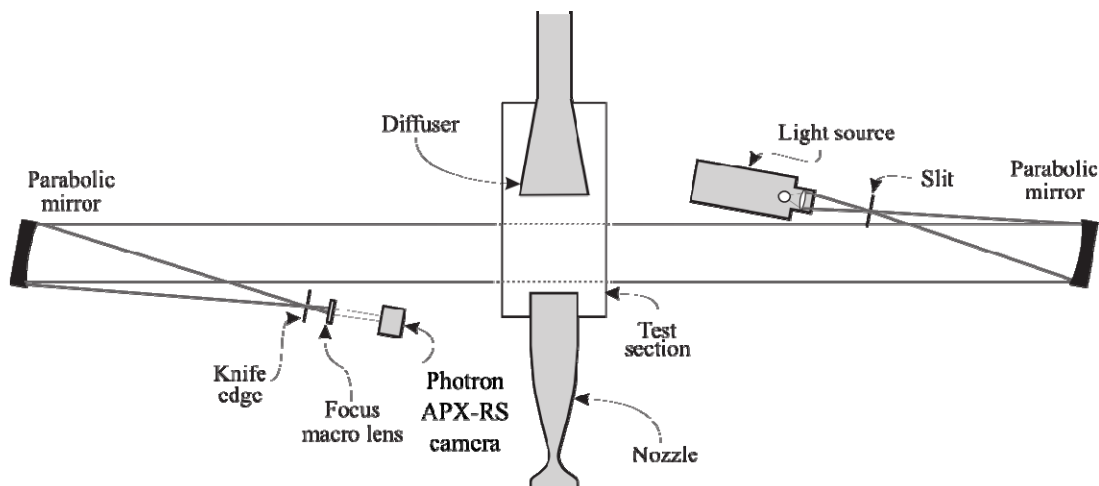


Figure 3. The assembly of micro-ramp with flat plate.



The Aero-Physics Laboratory of the University of Manchester is equipped with a Toepler’s z-type Schlieren system which consists of a Palflash 501 (Pulse Photonics) continuous light source with a focusing lens and a 2 mm wide slit, two $f = 9$ parabolic silver coated mirrors, a knife-edge and a Hoya 49 mm +2 macro lens for focusing purposes. To capture the images, a Canon digital SLR camera EOS-450D 12MP was used while a Photron APX-RS high-speed video camera was also employed for high-speed image recording at 10,000 fps. The schematic of the schlieren setup is shown in Figure 4.

Figure 4. Toepler’s z-type Schlieren setup.



2.4. Infrared Thermography

The infrared (IR) camera used for this investigation was a FLIR Thermacam SC 3000 Cooled System. It is capable of measuring temperatures ranging from -250 K to $1,730$ K with an accuracy of $\pm 2\%$ or ± 2 K. It is equipped with a GaAs QWIP detector with a resolution of 320×240 pixels and cooled to 70 K in less than 6 min. The recording frequency of the camera is 50 Hz. The camera has to be kept at ambient pressure and therefore mounted on top of the test section at an angle of 15° from the vertical plane as shown in Figure 5. The window on the top of the test section is specially made from Germanium (Ge), which is a commonly used material for infrared thermography. It has a high index of refraction and good IR transmission. The camera is connected to a dedicated PC to record and store the images. To determine the local heat transfer rate, \dot{q} the following thin-skin technique from Schülien [21] is used for a time span of $t_{min} < t < t_{max}$:

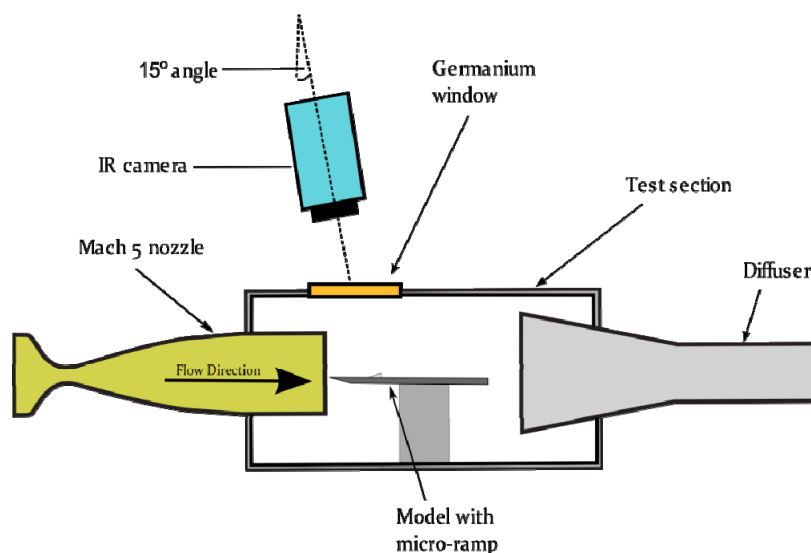
$$\dot{q} = \rho_m c_m d_m \frac{dT_w}{dt} \tag{1}$$

where ρ_m , c_m and d_m are the density, thermal heat capacity and wall thickness of the material, respectively. T_w represents the wall temperature measured by the infrared camera. The values of t_{min} and t_{max} were obtained from the steady run time of the HSST wind tunnel, excluding the tunnel start-up and shutting down time. T_w is the measured rise of the wall temperature. The thin-skin technique can be applied if the wall temperature normal to the model surface can be assumed uniform and the lateral heat conduction in the wall can be neglected. These conditions are attained if the thin-wall test model is manufactured from high thermal conductivity material such as copper, nickel, aluminum, etc. To non-dimensionalise \dot{q} , the following formula for the Stanton number, St was applied:

$$St = \frac{\dot{q}}{\rho_\infty U_\infty c_p (T_0 - T_w)} \tag{2}$$

where ρ_∞ and U_∞ are the density and velocity of the freestream flow, respectively. The specific heat capacity of air at constant pressure, c_p and the stagnation temperature, T_0 are measured by a k-type thermocouple located inside the settling chamber.

Figure 5. Experimental setup for infrared thermography.



The properties of the freestream flow conditions and material in this investigation applied in Equations (1) and (2) are listed in Tables 2 and 3, respectively.

Table 2. HSST flow condition during infrared thermography experiment measured directly from the wind tunnel.

Specific Heat (Air), C_{p-air}	1,007.81 Nm/kgK
Freestream Temperature, T_∞	62.79 K
Freestream Pressure, P_∞	1,354.93 Pa
Reynolds number, Re	$13.3 \times 10^6/m$
Total Temperature, T_0	376.74 K
Freestream Velocity, U_∞	785.69 m/s

Table 3. Properties of the material used in the infrared thermography experiment.

Material	Aluminium Alloy (Grade 6082)
Density, ρ_m	2,700 kg/m ³
Thermal Heat Capacity, C_m	896 J/kgK
Thermal Conductivity, λ_m	167 W/mK

2.5. Surface Flow Visualization

The oil flow recipe used in the current setup has been optimized for the current experimental conditions. This ensures that the oil does not dry too quickly, allowing sufficient time for the flow to establish, but at the same time it is not so viscous that it does not follow the flow streamlines. The mixture consists of paraffin, fluorescent color powders, silicon oil and oleic acid. The fluorescent powder used has an average grain size of 10 μm . Two Maplin Electronics UV light sources with a 20 W fluorescent tube of 600 mm length were mounted at a 45° angle on both sides of the test section windows to illuminate the mixture. Mounting the lights on both sides of the test section provided optimum illumination with minimum direct exposure to the camera. It also prevented shadows from occurring as a direct result from the model that would otherwise occur from using light on one side only.

A Digital SLR camera, Nikon D90 12.3 million pixels with 18–105 VR lens was used to record high-definition videos of the run. It is capable of recording 24fps video at a resolution of 1,280 \times 720. Individual images were then extracted from the video using VirtualDub, an open source software. Due to the position of the test section window, it was not possible to place the camera perpendicular to the surface of the flat plate. Therefore it was mounted at an angle of 20.8° from the vertical plane.

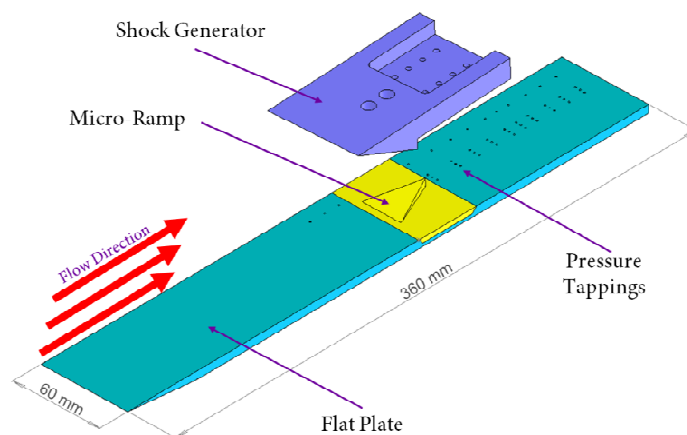
The flat plate and the micro-ramps were both painted matt-black to increase the contrast between the plate and the fluorescent oil. An area of 60 mm \times 60 mm was drawn 30 mm upstream from the micro-ramp leading edge to mark the location where the paint would be deposited. A 5 mL syringe was used to carefully apply the paint onto the model so that the paint did not spill and flow outside the dedicated boundary.

2.6. Shock-Generator Setup

To investigate the effectiveness of micro-ramps in controlling SBLI, an oblique shock wave needed to be generated and eventually impinged on the flat plate downstream the micro-ramp location. For

this reason a shock-generator was installed by mounting it to the ceiling plate of test section. The overall setup is shown in Figure 6. The shock-generator created a 34° oblique shock impinging at a location 14.2δ downstream the centre of micro-ramp which is exactly on the 4th row of pressure tappings. The installation denied the access of the optical windows of the tunnel and therefore only pressure measurements experiments were able to be conducted with this setup.

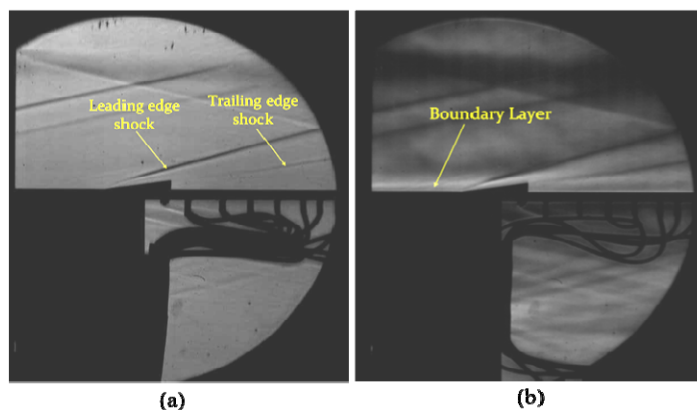
Figure 6. Overall setup including the shock generator.



3. Results and Discussion

From the schlieren photograph in Figure 7, an easily visible strong shock wave can be observed originating from the micro-ramp leading edge and a weaker shock wave can be seen at the trailing edge of the model. Note that the other shock waves that are visible are from the flat plate leading edge and the nozzle exit. The incoming boundary layer was only visible in the high-speed schlieren photograph shown in Figure 7, because the exposure time in normal schlieren is too long. The exposure time of the high-speed schlieren is 1 μ s compared to 250 μ s for normal schlieren. Sudden growth of the boundary layer is observed as it approaches the leading edge of the micro-ramp. From Figure 7, it can also be seen that the micro-ramp is submerged in the boundary layer, which satisfies the criterion of a micro vortex generator as explained in Section 1.

Figure 7. Schlieren images for model MR80. Normal schlieren (a) and high-speed schlieren at 10,000 fps (b) from Saad *et al.* [22] (Reprinted with permission of the American Institute of Aeronautics and Astronautics).



Comparing the shock structures of MR40 and MR80 in Figure 8, both of them appear to be similar. However, a thicker shock line originating from the leading edge of MR80 is observed compared to MR40 and this is the indication of a stronger shock due to the significant difference in the size of the models. Giving attention to the trailing edge shock for both models, again MR80 produces a slightly stronger shock whereas for MR40 is very weak and is barely visible. A bigger model deflects more flow because of a larger surface area; hence a stronger shock is needed.

Figure 8. Comparison of schlieren images of MR40 (a) and MR80 (b).

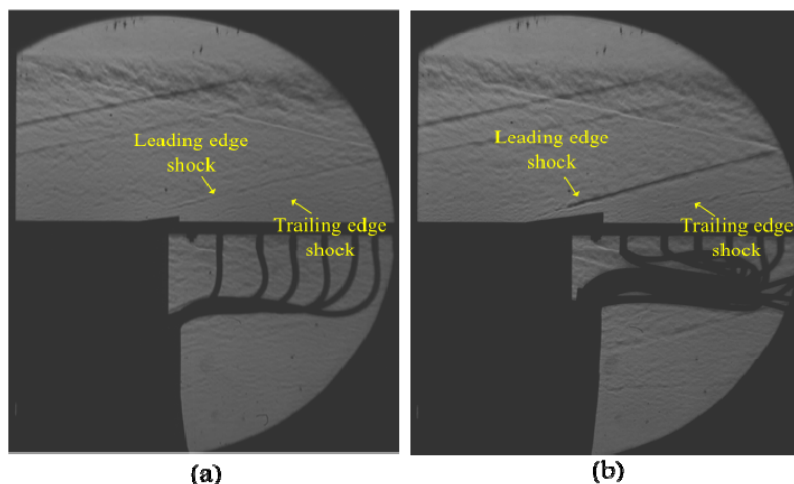


Figure 9 shows the images in chronological order of the surface flow visualization experiments for MR80. In the initial stage of the run, the oil blankets the entire micro-ramp surface with the flow. Heavy accumulation of oil is observed to occur at the micro-ramp's leading edge, and this is indication of flow separation, as can be seen in Figure 9(e). The separation is induced by the small leading angle which was measured to be 8.6° from the horizontal plane. The shock wave that was observed in the schlieren images in Figure 7 is also created by this angle.

The flow on the top surface of the micro-ramp moves towards the slant edges on both sides. This is caused by the high pressure induced by the leading-edge shock wave. This was also observed by Saad *et al.* [23] as shown in Figure 10. The flow moving down the slant edges in a rotational manner then forms the large vortices visible on both sides, named primary vortices. Downstream of the model there are two wide areas that are not covered with oil and this is known to be the trail of the primary vortices. The oil is prevented from accumulating on the surface by the motion of the vortices. The footprint starts to appear in the oil flow images 5 s after the run as shown in Figure 9(f). An upwash motion at the centerline is produced by the primary vortices, this is deduced from the direction of oil dots shown in Figure 10. Another pair of smaller vortices can be observed wrapping around the micro-ramp shown by the thin oil streak and known as the horseshoe vortex. Next, the thick band of oil in the centerline of the micro-ramp starts to divide into half, creating two small tube-like structures of oil traveling downstream shown in Figure 9(d). The separation can be seen clearly a few seconds later in Figure 9(f). These are called the secondary vortices. Finally, Figure 9(g,h) shows the oil being smeared by the terminating shock of the wind tunnel and the final condition of model, respectively.

Figure 9. Chronology of surface oil-flow experiments from Saad *et al.* [22] (Reprinted with permission of the American Institute of Aeronautics and Astronautics).

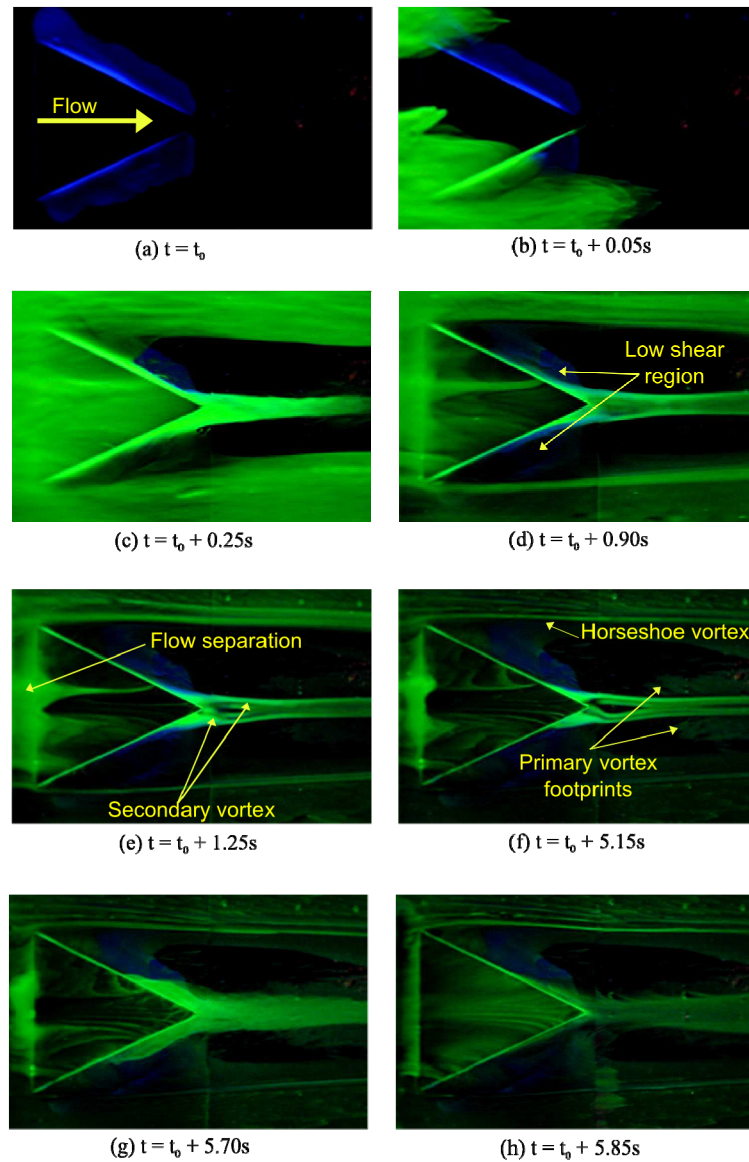


Figure 10. Oil-dot visualization results for Mach 5 flow by Saad *et al.* [23].

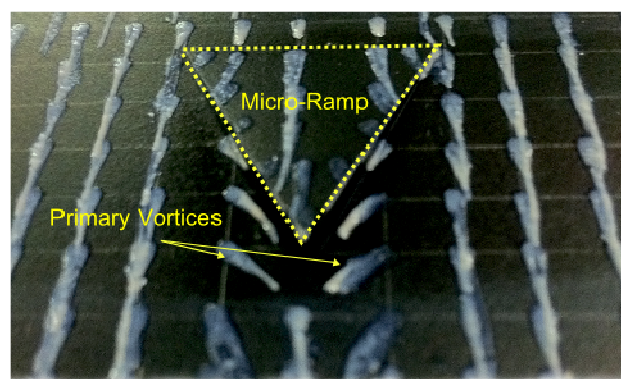


Figure 11 shows the surface flow visualization images of both models MR40 and MR80. The MR80 secondary vortices, near the centerline, are significantly bigger, and also a larger wake area is formed

downstream the model. The downstream area not covered by oil is also bigger, depicting the generation of a larger primary vortex. An efficient way of quantifying the relationship between the micro-ramps and their wake would be through a scaled analysis, requiring detailed measurements of the vortex size and structures formed in the wake at high resolution, which was not possible with the existing instrumentation. Near the MR80 leading edge a greater accumulation of oil is seen due to a larger separation region. Note that the traces of oil at the sides of the micro ramp for MR80 in Figure 11(a) are not because of the primary vortices footprints. Initially a small amount of oil was deposited around the model to clearly identify the location of the model, as can be seen in Figure 9(a). Surprisingly after the tunnel was operated and air was rushing through the nozzle exit, the oil was not blown away and remained at its position. This indicates the existence of a low shear region at the sides of the micro-ramp even though this coincides with the location where the primary vortices start to be generated. From this it can be speculated that the primary vortices start to touch the surface of the wall after a certain distance downstream from the leading edge.

Figure 11. Surface oil-flow visualization images of MR40 (a) and MR80 (b).

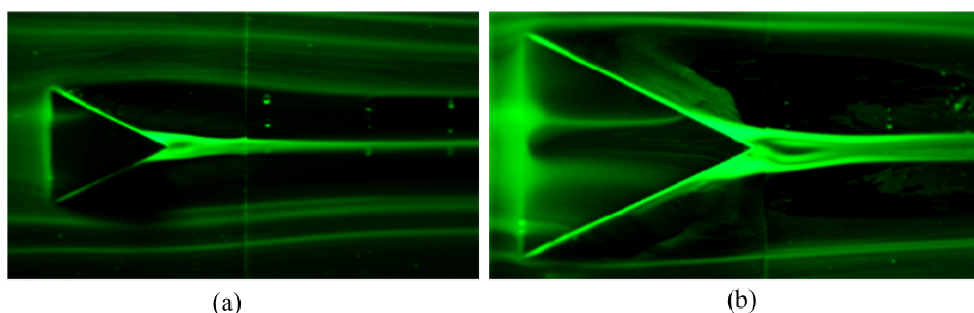
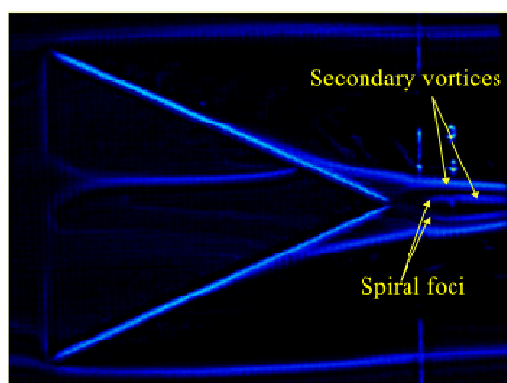


Figure 12. Surface flow visualization result of MR80 after being manipulated, from Saad *et al.* [22] (Reprinted with permission of the American Institute of Aeronautics and Astronautics).



Further image processing was performed using Davis 7.2 software from LaVision. The raw images were imported into Davis and a number of post processing algorithms including filtering were performed. By doing this, the flow structures became more visible as can be seen from Figure 12. Apart from the clearer structures of the horseshoe vortices and the secondary vortices mentioned before, another pair of secondary vortices can be observed located between the first pair of secondary vortices. They suddenly appear at 2.2δ downstream the apex of the micro-ramp, originating from a

point named spiral foci as found originally by Li & Liu [9,10] and later revealed in the experiments done by Lu *et al.* [16,17]. The bright line at the edge of the micro-ramp chord represents the separation line which stretches from the leading edge to the apex of the model.

Using Davis, the RMS of MR40 images was calculated and the result is shown in Figure 13(a). Details of the flow characteristics are identified. The schematic diagram representing the overall vortices system generated by the micro-ramp is shown in Figure 13(b). Overall there are four pairs of vortices in the system comprised of a pair of primary vortices and three pairs of secondary vortices including the horseshoe vortices.

Figure 13. Surface flow visualization image after processing and the generation of schematic representation of the vortices.

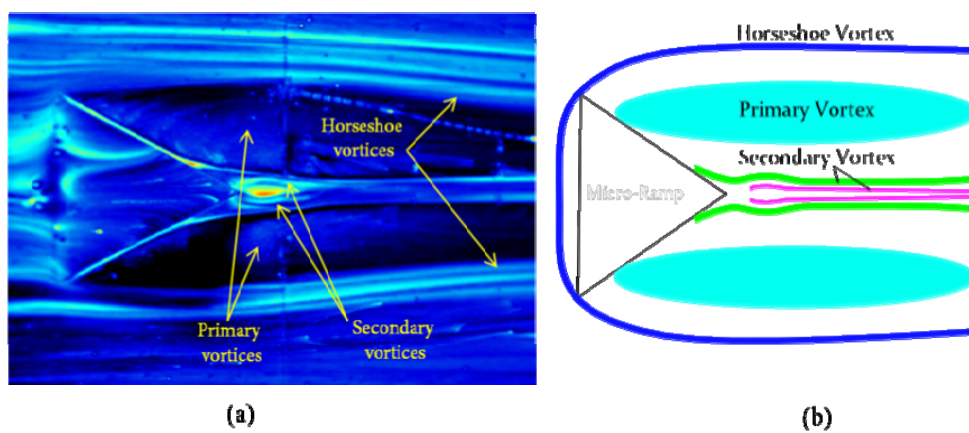
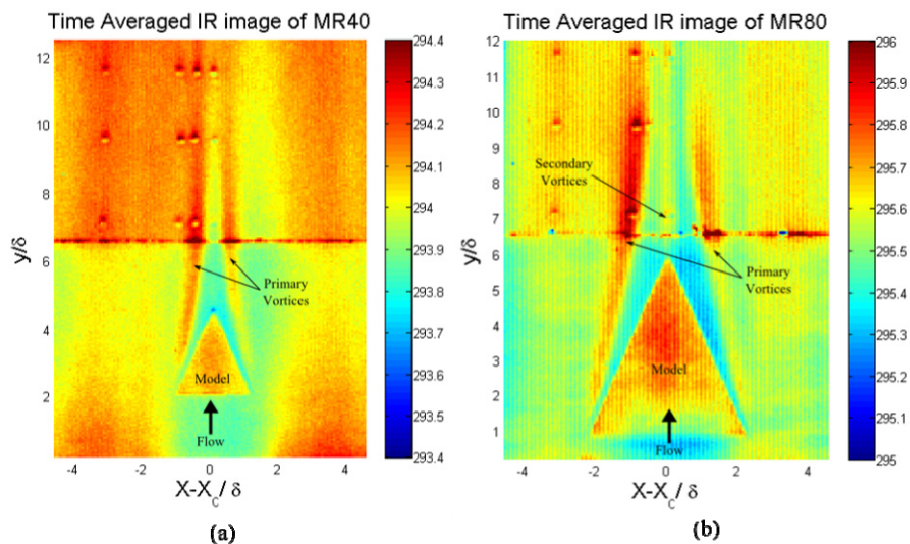


Figure 14. Surface temperature map from infrared thermography for MR40 (a) and MR80 (b).



The IR images mapping the surface temperature of the flat plate of both models are shown in Figure 14. The different sizes of primary vortices for the two models can be seen. It can also be seen that the primary vortices originate 0.5δ after the leading edge of the micro ramp. As the vortices develop downstream they grow larger, represented by larger streaks in Figure 14(a,b). The secondary vortices observed in Figure 13, can also be seen in Figure 14(a). They suddenly appear in between the location of the primary vortices and stretch downstream. This is identified by a slightly higher

temperature streak that starts at a location approximately 0.4δ downstream of the apex of the micro-ramp. However, the same feature is not visible in Figure 14(b) for the MR40 model. This is believed to be due to weaker and smaller vortices being produced that cannot be captured by the IR camera. Therefore a higher spatial resolution is required in order to assess this. The plot of the Stanton number at a profile line 0.5δ downstream of the micro-ramp apex is shown in Figure 15. There are two peaks identified for each plot representing the primary vortices generated. The Stanton number at the location of the vortices relative to the freestream flow is higher for MR80. This implies that MR80 produces stronger vortices that transfer more heat to the surface.

Figure 15. The plot of Stanton number along a profile line 0.5δ downstream of the micro-ramp apex.

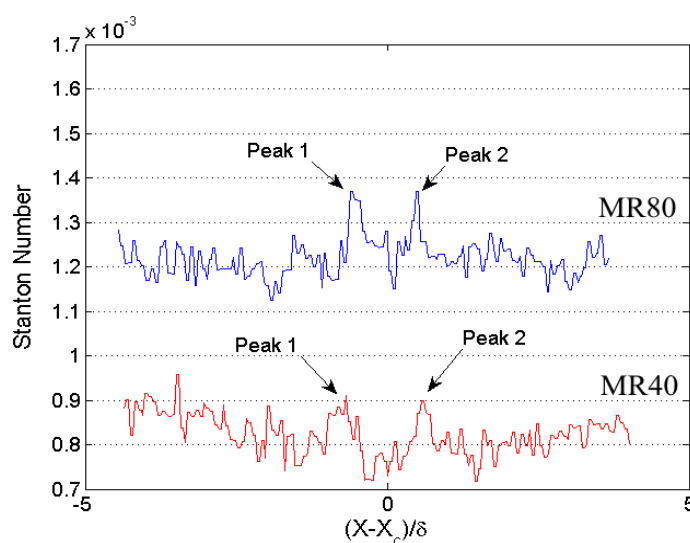
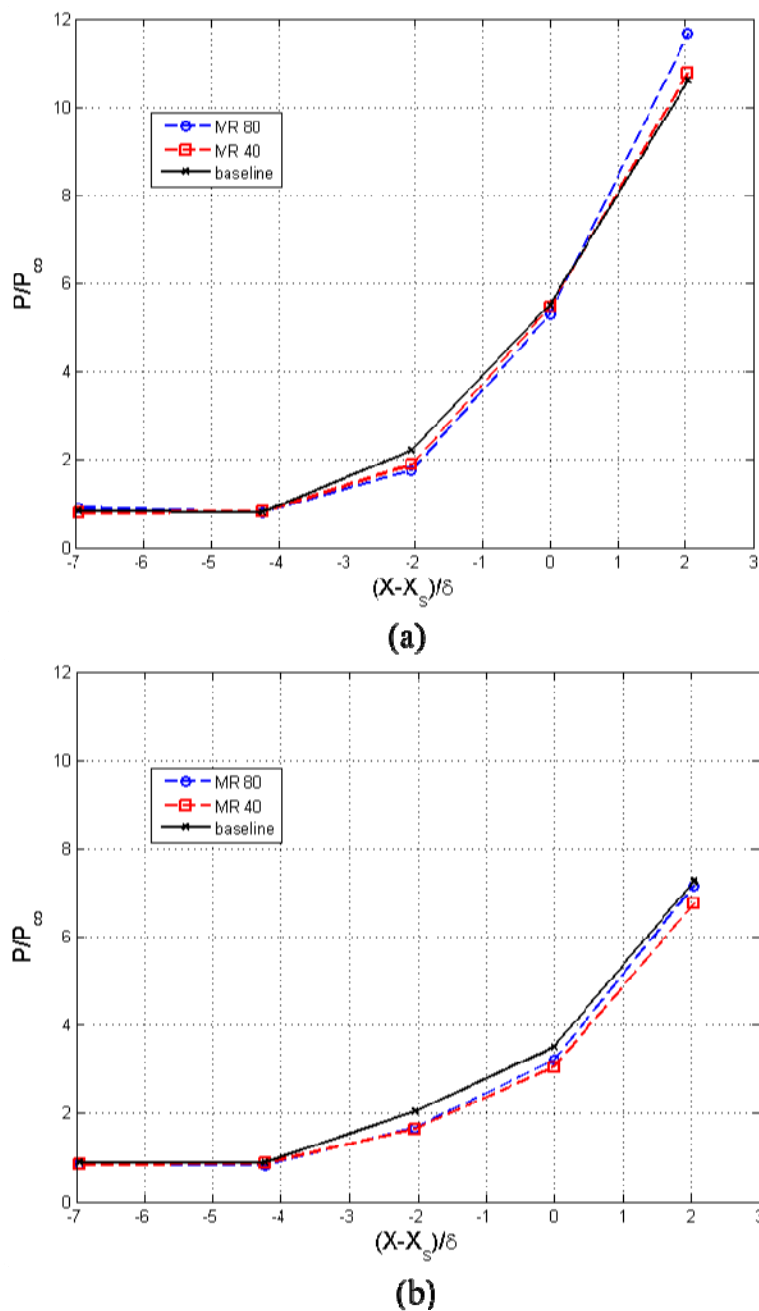


Figure 16 presents the pressure measurements downstream the micro-ramp at the centerline and off-center position of $z = 20$ mm with an impinging oblique shock wave. The error was calculated to be 1.8% from the baseline value. For both locations, the comparison between the baseline case (clean tunnel) and the cases with micro-ramps shows that the presence of micro-ramp proved to delay the pressure rise caused by the impinging shock or in other words managed to reduce the upstream interaction length as mentioned by Delery [1] and Delery *et al.* [24]. Note that X_s is the location of shock impingement as described in Section 2.6 and is represented by $X = 0$ in Figure 16. To measure the effectiveness of each micro-ramp, the area under the graph in Figure 16(a) was calculated to quantify the improvement made. The MR80 model reduced the pressure rise associated with the baseline configuration by up to 17%. Comparing the effect of different sizes, model MR40 managed to reduce the upstream interaction length up to 14% from the baseline case. Here we can see that the difference between MR40 and MR80 is just 3%, a small amount compared to the size, which is double from each other. Therefore, since almost identical improvements can be made using the smaller micro-ramp, which is also half the weight of the larger one, it can be concluded that using the smaller model will lead to beneficial flow control with the benefit of weight saving and decrease in drag penalty. It is also essential to mention that the increase in pressure gradient from the beginning, and the higher pressure reading at $X = 2$ observed from MR80 is believed to be a positive sign of the suppression of the boundary layer separation. This was also shown in the findings by Babinsky *et al.* [11].

Figure 16. Streamwise surface pressure measurements at centerline (a) and $z = 20$ mm (b) with shock incident at 14.2δ downstream the mid-chord of MR40 and MR80.



4. Conclusions

The current study extends the scope of collective research efforts done on micro-ramps by subjecting it to a Mach 5 flow. The flow structures over the micro-ramps were characterized qualitatively and quantitatively using different experimental techniques. Schlieren images showed the basic shock structures associated with the presence of the micro-ramps and the height of the micro-ramp compared to the boundary layer. As expected, the micro-ramp was shown to be fully immersed inside the boundary layer and validated the term ‘micro’. At least four pairs of vortices with different sizes were shown to be present in the surface flow visualisation. The separation region upstream of micro-ramp was captured using infrared thermography. Only the pair of primary vortices

could be observed using this method. The pressure measurement proved that the presence of micro-ramps reduces the upstream interaction length by delaying the pressure rise, hence suppressing the SBLIs effect. Overall, the experimental work done in the study has shown great potential in contributing more to the general understanding of the basic flow physics associated with micro-ramps and their effect in controlling SBLIs.

Acknowledgments

The authors would like to thank K. Kontis for his valuable advice and supervision. Special thanks to the members of the Aero-Physics Laboratory for their generous sharing of experiences and knowledge. Also to the Universiti Pertahanan Nasional Malaysia (UPNM) and the Ministry of Higher Education of Malaysia for the research sponsorship. Finally to the technical staff of the University of Manchester for their assistance.

References

1. Delery, J.M. Shock/wave/turbulent boundary layer interaction and its control. *Prog. Aerosp. Sci.* **1985**, *22*, 209–280.
2. Dolling, D.S. Fifty years of shock-wave/boundary-layer interaction research: What next? *AIAA J.* **2001**, *39*, 1517–1532.
3. McCormick, D.C. Shock/boundary layer interaction control with vortex generators and passive cavity. *AIAA J.* **1993**, *31*, 91–96.
4. Holden, H.; Babinsky, H. Effect of microvortex generators on separated normal shock/boundary layer interactions. *J. Aircr.* **2007**, *44*, 170–174.
5. Lin, J.C. Review of research on low-profile vortex generators to control boundary layer separation. *Prog. Aerosp. Sci.* **2002**, *38*, 389–420.
6. Ashill, P.R.; Fulker, J.L.; Hackett, K.C. Research at DERA on sub-boundary layer vortex generators (SBVG). In *Proceedings of the 39th AIAA Aerospace Sciences Meeting and Exhibit*, Reno, NV, USA, 8–11 January 2001; AIAA Paper 2001-0887.
7. Anderson, B.H.; Tinapple, J.; Surber, L. Optimal control of shock wave turbulent boundary layer interactions using micro-array actuation. In *Proceedings of the 3rd AIAA Flow Control Conference*, San Francisco, CA, USA, 5–8 June 2006; AIAA Paper 2006-3197.
8. Blinde, P.L.; Humble, R.A.; van Oudheusden, B.W.; Scarano, F. Effects of micro-ramps on a shock wave/turbulent boundary layer interaction. *Shock Waves* **2009**, *19*, 507–520.
9. Li, Q.; Liu, C. LES for supersonic ramp control flow using MVG at $M = 2.5$ and $Re_\theta = 1,440$. In *Proceedings of the 48th AIAA Aerospace Sciences Meeting Including the New Horizons Forum and Aerospace Exposition*, Orlando, FL, USA, 4–7 January 2010; AIAA Paper 2010-0592.
10. Li, Q.; Liu, C. Numerical investigations on the effects of the declining angle of the trailing-edge of MVG. In *Proceedings of the 27th AIAA Aerodynamic Measurement Technology and Ground Testing Conference*, Chicago, IL, USA, 28 June–1 July 2010; AIAA Paper 2010-4623.
11. Babinsky, H.; Li, Y.; Pitt Ford, C.W. Microramp control of supersonic oblique shock-wave/boundary-layer interactions. *AIAA J.* **2009**, *47*, 668–675.

12. Wang, K.C. Boundary layer over a blunt body at high incidence with an open-type of separation. *Proc. R. Soc. Lond. A* **1974**, *340*, 33–35.
13. Yan, Y.; Chen, C.; Wang, X.; Liu, C. Study on mechanism of ring generation behind supersonic MVG. In *Proceedings of the 50th AIAA Aerospace Sciences Meeting including the New Horizons Forum and Aerospace Exposition*, Nashville, TN, USA, 9–12 January 2012; AIAA Paper 2012-1093.
14. Lu, P.; Yan, Y.; Liu, C. Numerical study on mechanism of multiple rings formation. In *Proceedings of the 50th AIAA Aerospace Sciences Meeting including the New Horizons Forum and Aerospace Exposition*, Nashville, TN, USA, 9–12 January 2012; AIAA Paper 2012-0747.
15. Yan, Y.; Chen, C.; Wang, X.; Liu, C. The interaction between vortex rings and oblique shocks by the MVG controlled ramp flow at $M = 2.5$. In *Proceedings of the 50th AIAA Aerospace Sciences Meeting including the New Horizons Forum and Aerospace Exposition*, Nashville, TN, USA, 9–12 January 2012; AIAA Paper 2012-0047.
16. Lu, F.L.; Pierce, A.J.; Shih, Y.; Liu, C.; Li, Q. Experimental and numerical study of flow topology past micro vortex generators. In *Proceedings of the 27th AIAA Aerodynamic Measurement Technology and Ground Testing Conference*, Chicago, IL, USA, 28 June–1 July 2010; AIAA Paper 2010-4463.
17. Lu, F.L.; Pierce, A.J.; Shih, Y. Experimental study of near wake of micro vortex generators in supersonic flow. In *Proceedings of the 27th AIAA Aerodynamic Measurement Technology and Ground Testing Conference*, Chicago, IL, USA, 28 June–1 July 2010; AIAA Paper 2010-4623.
18. Sun, Z.; Schrijer, F.F.K.; Scarano, F.; Oudheusden, B.W.V. PIV Investigation of the 3D instantaneous flow organization behind a micro-ramp in a supersonic boundary layer. In *Shock Waves*; Kontis, K., Ed.; Springer: Heidelberg, Germany, 2011.
19. Erdem, E.; Kontis, K. Non-Plasma and plasma transverse jets in hypersonic cross flow. In *Proceedings of the 16th AIAA/DLR/DGLR International Space Planes and Hypersonic Systems and Technologies Conference*, Bremen, Germany, 19–22 October 2009; AIAA Paper 2009-7253.
20. Yang, L.; Erdem, E.; Kontis, K. Pressure-sensitive paint visualization on double ramp in hypersonic flow. In *Proceedings of the 14th International Symposium on Flow Visualization*, Daegu, Korea, 21–24 June 2010.
21. Schülien, E. Skin-friction and heat flux measurements in shock/boundary layer interaction flows. *AIAA J.* **2006**, *44*, 1732–1741.
22. Saad, M.R.; Che Idris, A.; Zare-Behtash, H.; Kontis, K. Micro-Ramps in Mach 5 hypersonic flow. In *Proceedings of the 50th AIAA Aerospace Sciences Meeting including the New Horizons Forum and Aerospace Exposition*, Nashville, TN, USA, 9–12 January 2012; AIAA Paper 2012-0676.
23. Saad, M.R.; Erdem, E.; Yang, L.; Kontis, K. Experimental studies on micro-ramps in Mach 5. In *Shock Waves*; Kontis, K., Ed.; Springer: Heidelberg, Germany, 2011.
24. Delery, J.M.; Dussauge, J.P. Some physical aspects of shock-wave/boundary layer interactions. *Shock Waves* **2009**, *19*, 453–468.